XIV International Conference on Computational Plasticity. Fundamentals and Applications
COMPLAS XIV
E. Oñate, D.R.J. Owen, D. Peric & M. Chiumenti (Eds)

INVERSE FORM FINDING WITH H-ADAPTIVITY AND AN APPLICATION TO A NOTCH STAMPING PROCESS

M. CASPARI*,†, P. LANDKAMMER† AND P. STEINMANN†

† Institute of Applied Mechanics
Friedrich-Alexander University Erlangen-Nuremberg
Egerlandstr. 5, 91058 Erlangen, Germany
*e-mail: michael.caspari@fau.de
web page: http://www.ltm.uni-erlangen.de; http://www.tr-73.de

Key words: Inverse form finding, Shape optimization, H-adaptivity, Metal forming

Abstract. The aim is to determine the optimized semi-finished workpiece geometry to its given target geometry after a forming process. Hereby, a novel approach for inverse form finding, a type of a shape optimization, is applied to a notch stamping process. As a special feature, h-adaptive mesh refinement is considered within the iteratively performed forming simulation.

1 INTRODUCTION

Metal forming processes are classified into sheet forming with plane stress conditions and bulk metal forming with three dimensional stress conditions. Recently a new class of forming process called Sheet-Bulk Metal Forming (SBMF) has been introduced by [9]. SBMF combines three dimensional plastic flow with sheet metal forming operations, whereby the focus is placed on functional integration. It gains to form local shape elements normal to the sheet plane with a magnitude similar to the original sheet thickness. This leads to even higher requirements in regards to shape optimization. Numerical shape optimization is beneficial to reduce experimental costs, since trail-and-error methods and subsequent finishing operation steps, respectively, are minimized. In this contribution, shape optimization is applied by means of an inverse form finding strategy.

According to Chenot et. al. [4], the forming simulation, with quantities prescribed in the material configuration, is defined as a direct problem. Whereby shape optimization is referred to an inverse problem, which seeks to determine the optimal workpiece geometry based on the prescribed forming process and a target geometry.

For this purpose, a parameter-free (node-based), form finding algorithm is introduced by Landkammer and Steinmann [8]. It includes nodal positions as design variables and an objective function as minimization criterion. An iterative optimization strategy to update the workpiece geometry is implemented in a non-invasive fashion. This implicates independence of the algorithm to the constitutive behavior and the simulation tool. The

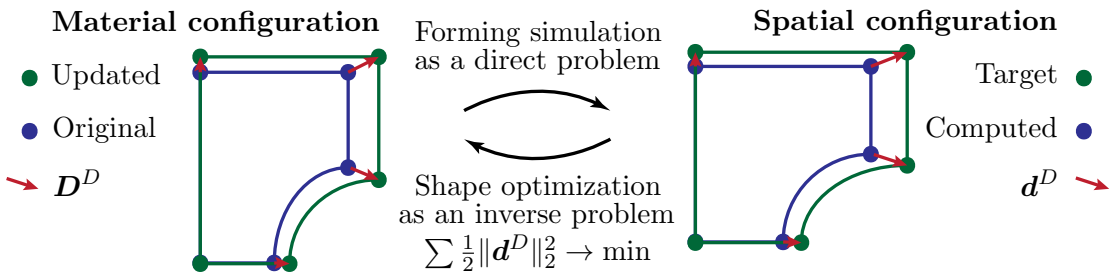

Figure 1: Inverse shape optimization procedure with material configuration, target spatial configuration and the computed spatial configuration

procedure is realized via subroutines, which translate information between the forming simulation (direct problem) and the optimization algorithm (indirect problem), see Fig. 1.

Shape optimization suffers from the contradiction to be efficient but accurate in same time. Due to large deformations within the forming simulation, a fine mesh is required in order to avoid serve mesh distortions of the finite element (FE) mesh. Adaptive strategies are required to decrease computational costs and minimize the discretization error. Here, an h-adaptive strategy is applied to locally refine the mesh during the simulation. It leads to a refinement of highly exposed regions and an efficient mesh is generated.

The implementation of adaptive remeshing techniques requires detailed investigation due to the applied node-based optimization strategy. The challenge of the inverse optimization process with h-adaptivity is caused by newly emerging nodes and elements within the model. This issue can be mastered by adjusting the subroutines, which translates information between the forming simulation (direct problem) and the optimization algorithm (inverse problem).

Due to the advantages of h-adaptivity, it is possible to optimize more complex geometries and to cope with large plastic strains. It even enables to include penetration of a sharp edge tool into the forming simulation.

The paper is structured as follows: In the sequel, basics of nonlinear continuum mechanics are introduced in Sec. 2 and FE discretization clarification is outlined in Sec. 3. The detailed algorithm for inverse form finding, formulated as an optimization problem, follows in Sec. 4. Afterwards, h-adaptive mesh refinement is described in Sec. 5. A example in Sec. 6, is presented to demonstrate the application of the mesh adaptivity within inverse form finding. Finally, Sec. 7 recaps the findings.

2 BASICS OF NONLINEAR CONTINUUM MECHANICS

A general description of nonlinear continuum mechanics is required for a discussion regarding inverse shape optimization and further the description of the h-adaptive refinement strategy. More detailed description of nonlinear continuum mechanics can be found in [1] among others.

2.1 Kinematics

Fig. 2 depicts a continuous setting of the material configuration $\mathcal{B}_0$ at time $t = 0$ and the spatial configuration $\mathcal{B}_t$ at time $t > 0$. A placement of a physical body into the Euclidean space $\mathbb{E}^3$ with $\boldsymbol{E}_i \equiv \boldsymbol{e}_i$ and $i = 1, 2, 3$ is assumed.

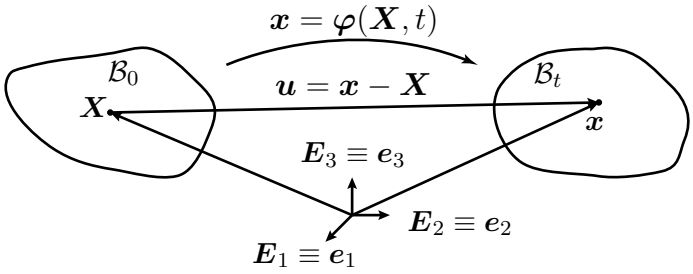

Figure 2: Kinematics of a nonlinear continuum with the undeformed (material) and the deformed (spatial) configuration

The deformation map $\boldsymbol{\varphi}$ maps positions $\boldsymbol{X}$ of a material configuration $\mathcal{B}_0$ to positions $\boldsymbol{x}$ of a spatial (deformed) configuration $\mathcal{B}_t$:

$$\boldsymbol{x} = \boldsymbol{\varphi}(\boldsymbol{X}, t) \quad : \mathcal{B}_0 \to \mathcal{B}_t \tag{1}$$

The displacement field $\boldsymbol{u}$ occurs to the difference of the position vectors at spatial and material configurations:

$$\boldsymbol{u}(\boldsymbol{X}, t) = \boldsymbol{\varphi}(\boldsymbol{X}, t) - \boldsymbol{X} \tag{2}$$

The gradient $\boldsymbol{F}$ of the deformation map with respect to material coordinates renders a linear map from the material tangent space $T\mathcal{B}_0$ to the spatial tangent space $T\mathcal{B}_t$:

$$\boldsymbol{F} = \frac{\partial \boldsymbol{\varphi}(\boldsymbol{X})}{\partial \boldsymbol{X}} \quad : T\mathcal{B}_0 \to T\mathcal{B}_t \tag{3}$$

2.2 Weak Piola formulation

In the following, the body forces are neglected due to its minor influence in contrast to forming forces.

An equilibrium in the Piola formulation is given by the boundary value problem with Dirichlet and Neumann boundary conditions (Eq. 5):

$$\mathrm{Div}\boldsymbol{P} = \boldsymbol{0} \tag{4}$$

$$\boldsymbol{\varphi} = \bar{\boldsymbol{\varphi}} \quad \text{on} \quad \partial\mathcal{B}_0^{\boldsymbol{\varphi}} \qquad \text{and} \qquad \boldsymbol{P} \cdot \boldsymbol{N} = \boldsymbol{T} \quad \text{on} \quad \partial\mathcal{B}_0^{\boldsymbol{T}} \tag{5}$$

The balance equation (Eq. 4), formulated with the first Piola-Kirchhoff stress $\boldsymbol{P}$, results from the balance of linear momentum, including the divergence operator with respect to material coordinates.

This system of equations is solved by an application of the principle of virtual work. Therefore, virtual displacements $\delta\boldsymbol{\varphi}$ are introduced. With corresponding initial conditions, the weak formulation is written as:

$$\int_{\mathcal{B}_0} \boldsymbol{P} : \delta\boldsymbol{F}\mathrm{d}V = \int_{\partial\mathcal{B}_0^t} \delta\boldsymbol{\varphi} \cdot \boldsymbol{T}\mathrm{d}A \qquad \forall\delta\boldsymbol{\varphi} \text{ admissible} \tag{6}$$

3 FINITE ELEMENT DISCRETIZATION

Discretization is required to solve the weak formulation in Eq. 6 for a continuum body $\mathcal{B}$. The body itself and likewise the field values are approximated. Gauss-integration is typically performed for solving integrals over a finite element. Linearization enables the use of efficient iterative solution methods for the system of nonlinear equations.

3.1 Discretization of a body into finite elements

The body $\mathcal{B}$ is discretized into n_{elem} elements:

$$\mathcal{B}_0 \approx \mathcal{B}_0^{\text{h}} = \bigcup_{e=1}^{n_{\text{elem}}} \mathcal{B}_0^e \qquad \text{and} \qquad \mathcal{B}_t \approx \mathcal{B}_t^{\text{h}} = \bigcup_{e=1}^{n_{\text{elem}}} \mathcal{B}_t^e \tag{7}$$

Accordingly, coordinates of material and spatial configurations are prescribed as discretized values through:

$$\boldsymbol{X}^{\text{h}} = \bigcup_{e=1}^{n_{\text{elem}}} \boldsymbol{X}^e \qquad \text{and} \qquad \boldsymbol{x}^{\text{h}} = \bigcup_{e=1}^{n_{\text{elem}}} \boldsymbol{x}^e \tag{8}$$

Within the isoparametric concept, all kinematic quantities are approximated by the same shape functions $N^i(\boldsymbol{\xi})$ for each element node ($i = 1 \dots n_{\text{en}}$), which are defined on a reference element $\mathcal{B}_\square$ with isoparametric coordinates $\boldsymbol{\xi} \in [-1, 1]^{n_{\text{dim}}}$. The element coordinates $\boldsymbol{X}^e$ and $\boldsymbol{x}^e$ depend on the nodal positions $\boldsymbol{X}^i$ and $\boldsymbol{x}^i$:

$$\boldsymbol{X}^e(\boldsymbol{\xi}) = \sum_{i=1}^{n_{\text{en}}} \boldsymbol{X}^i N^i(\boldsymbol{\xi}) \qquad \text{and} \qquad \boldsymbol{x}^e(\boldsymbol{\xi}) = \sum_{i=1}^{n_{\text{en}}} \boldsymbol{x}^i N^i(\boldsymbol{\xi}) \tag{9}$$

The deformation map and further the deformation gradient follows the discretization with:

$$\boldsymbol{x}^{\text{h}} = \boldsymbol{\varphi}(\boldsymbol{X}^{\text{h}}, t) \quad : \mathcal{B}_0^{\text{h}} \to \mathcal{B}_t^{\text{h}} \quad \text{and} \quad \boldsymbol{F}^{\text{h}} = \frac{\partial\boldsymbol{\varphi}(\boldsymbol{X}^{\text{h}})}{\partial\boldsymbol{X}^{\text{h}}} \quad : T\mathcal{B}_0^{\text{h}} \to T\mathcal{B}_t^{\text{h}} \tag{10}$$

The Jacobians

$$\boldsymbol{J}^e(\boldsymbol{\xi}) = \sum_{i=1}^{n_{\text{en}}} \boldsymbol{X}^i \otimes \frac{\partial N^i(\boldsymbol{\xi})}{\partial\boldsymbol{\xi}} \qquad \text{and} \qquad \boldsymbol{j}^e(\boldsymbol{\xi}) = \sum_{i=1}^{n_{\text{en}}} \boldsymbol{x}^i \otimes \frac{\partial N^i(\boldsymbol{\xi})}{\partial\boldsymbol{\xi}} \tag{11}$$

are used for the mapping from the reference element to the element of spatial or material configuration. The deformation gradient $\boldsymbol{F}^e$ yields:

$$\boldsymbol{F}^e(\boldsymbol{\xi}) = \boldsymbol{j}^e(\boldsymbol{\xi}) \cdot \boldsymbol{J}^e(\boldsymbol{\xi})^{-1} = \left[\sum_{i=1}^{n_{\text{en}}} \boldsymbol{x}^i \otimes \frac{\partial N^i(\boldsymbol{\xi})}{\partial \boldsymbol{\xi}}\right] \cdot \left[\sum_{i=1}^{n_{\text{en}}} \boldsymbol{X}^i \otimes \frac{\partial N^i(\boldsymbol{\xi})}{\partial \boldsymbol{\xi}}\right]^{-1} \tag{12}$$

Relations between an element in material, spatial and reference configuration are depicted in Fig. 3.

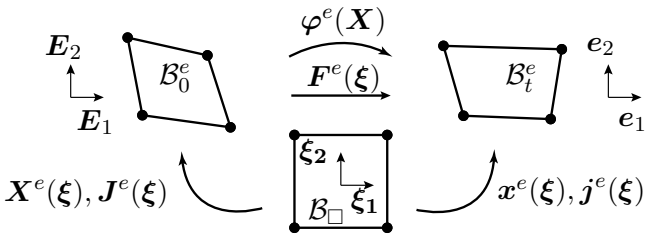

Figure 3: Mapping of a reference element to the material and the spatial configuration.

3.2 Discretization and linearization of the weak formulation

Neglecting dynamics, the weak formulation (Eq. 6) contains internal and external virtual work. The prescribed discretization and linearization is required and demonstrated exemplary for the internal virtual work.

$$\begin{aligned} \delta W_{0\,\text{int}} &= \int_{\mathcal{B}_0} \left[\boldsymbol{F}^{\mathsf{T}} \cdot \frac{\partial\, \delta\boldsymbol{\varphi}}{\partial \boldsymbol{X}}\right]^{\text{sym}} : \boldsymbol{S}\mathrm{d}V \\ &\approx \delta W_{0\,\text{int}}^{\text{h}} = \delta\boldsymbol{\varphi}^I \mathop{\mathsf{A}}_{e=1}^{n_{\text{elem}}} \int_{\mathcal{B}_0^e} \boldsymbol{F} \cdot \boldsymbol{S} \cdot \frac{\partial N^i}{\partial \boldsymbol{X}} \mathrm{d}V^e = \delta\boldsymbol{\varphi}^I \cdot \boldsymbol{f}_{\text{int}}^I \end{aligned} \tag{13}$$

Hereby $\delta\boldsymbol{\varphi}$ denotes the virtual displacement, discretized in the same way as the deformation map (Eq. 9), which is referred to as the Galerkin Method. The same procedure for external virtual work results in an external force vector:

$$\boldsymbol{f}_{\text{ext}}^I = \mathop{\mathsf{A}}_{e=1}^{n_{\text{elem}}} \int_{\delta\mathcal{B}_0^e} N^i \bar{\boldsymbol{T}}\, \mathrm{d}A^e \tag{14}$$

This leads further to a system of equations which is represented node wise as:

$$\boldsymbol{r}^I = \boldsymbol{f}_{\text{int}}^I - \boldsymbol{f}_{\text{ext}}^I = \boldsymbol{0} \qquad \forall I = 1, ..., n_{\text{nodes}} \tag{15}$$

The residuum $\boldsymbol{r}_I$ has to be solved for each node I. For a solution, the linearization of this equation is needed. It consequently follows for one element:

$$\delta\boldsymbol{\varphi}^{e\mathsf{T}} \cdot \boldsymbol{K}^e \cdot \Delta\boldsymbol{\varphi}^e = \delta\boldsymbol{\varphi}^{e\mathsf{T}} \cdot \boldsymbol{f}^e \tag{16}$$

4 INVERSE FORM FINDING

A node-based approach is pursued to solve the inverse form finding problem. Therefore, coordinates of selected design nodes serve as design variables for the optimization algorithm, introduced by [8].

The objective function

$$\delta(\mathbf{X}^{\mathrm{D}}, \mathbf{x}^{\mathrm{D}}_{\mathrm{tg}}) = \sum_{D=1}^{n_{\mathrm{dsgn}}} \delta^D \left(\boldsymbol{x}^D_{\mathrm{tg}}, \boldsymbol{\varphi}(\boldsymbol{X}^D) \right) \tag{17}$$

summarizing the local squared error

$$\delta^D = \frac{1}{2}\, \boldsymbol{d}^{D\mathsf{T}} \cdot \boldsymbol{d}^D \tag{18}$$

with nodal differences

$$\boldsymbol{d}^D = \boldsymbol{x}^D_{\mathrm{tg}} - \boldsymbol{\varphi}(\boldsymbol{X}^D) \tag{19}$$

between the current spatial configuration $\boldsymbol{\varphi}(\boldsymbol{X}^D)$ and the prescribed target positions $\boldsymbol{x}^D_{\mathrm{tg}}$ determined at each design node $D = 1, \ldots, n_{\mathrm{dsgn}}$. The positions are stored in the column vectors $\mathbf{X}^{\mathrm{D}} = \left[\boldsymbol{X}^{1\top} \cdots \boldsymbol{X}^{n_{\mathrm{dsgn}}\top} \right]^\top$ and $\mathbf{x}^{\mathrm{D}} = \left[\boldsymbol{x}^{1\top} \cdots \boldsymbol{x}^{n_{\mathrm{dsgn}}\top} \right]^\top$.

The optimization strategy results in a minimization of the objective function, which is satisfied at the optimal configuration:

$$\left. \frac{\partial \delta(\mathbf{X}^{\mathrm{D}}, \mathbf{x}^{\mathrm{D}}_{\mathrm{tg}})}{\partial \mathbf{X}^{\mathrm{D}}} \right|_{\mathbf{X}^{\mathrm{D}}_{\mathrm{opt}}} \stackrel{!}{=} \mathbf{0} \tag{20}$$

In use of the approximation by Taylor series, Eq. 20 reads:

$$\frac{\partial \delta\left(\mathbf{X}^{\mathrm{D}}, \mathbf{x}^{\mathrm{D}}_{\mathrm{tg}}\right)}{\partial \mathbf{X}^{\mathrm{D}}} + \frac{\partial^2 \delta\left(\mathbf{X}^{\mathrm{D}}, \mathbf{x}^{\mathrm{D}}_{\mathrm{tg}}\right)}{\partial \mathbf{X}^{\mathrm{D}} \partial \mathbf{X}^D} \cdot \left[\mathbf{X}^{\mathrm{D}}_{\mathrm{opt}} - \mathbf{X}^{\mathrm{D}} \right] \stackrel{!}{=} \mathbf{0}\,, \tag{21}$$

The Taylor series is terminated after the first term. This leads to an iteration step as:

$$\mathbf{X}^{\mathrm{D}}_{k+1} = \mathbf{X}^{\mathrm{D}}_k - \frac{\partial^2 \delta\left(\mathbf{X}^{\mathrm{D}}, \mathbf{x}^{\mathrm{D}}_{\mathrm{tg}}\right)^{-1}}{\partial \mathbf{X}^{\mathrm{D}} \partial \mathbf{X}^{\mathrm{D}}} \cdot \frac{\partial \delta\left(\mathbf{X}^{\mathrm{D}}, \mathbf{x}^{\mathrm{D}}_{\mathrm{tg}}\right)}{\partial \mathbf{X}^{\mathrm{D}}} \tag{22}$$

Motivated by the mentioned node-wise optimization approach, Eq. 22 is written as an iteration step for each design node as:

$$\boldsymbol{X}^D_{k+1} = \boldsymbol{X}^D_k - \alpha\, \frac{\partial^2 \delta^D\left(\boldsymbol{X}^D, \boldsymbol{x}^{\mathrm{h}}_{\mathrm{tg}}\right)^{-1}}{\partial \boldsymbol{X}^D \partial \boldsymbol{X}^D} \cdot \frac{\partial \delta^D\left(\boldsymbol{X}^D, \boldsymbol{x}^{\mathrm{h}}_{\mathrm{tg}}\right)}{\partial \boldsymbol{X}^D} \tag{23}$$

This iteration includes a linesearch parameter α, controlled by Armijo-Backtracking [7], which ensures a suited update without serve mesh distortions. A complete update step is now written as:

$$\boldsymbol{X}^D_{k+1} = \boldsymbol{X}^D_k - \alpha\, \tilde{\boldsymbol{F}}^{D-1} \cdot \boldsymbol{d}^D \tag{24}$$

Table 1: The node-based optimization problem for inverse form finding [7].

Objective funct.:	$\delta\big(\mathbf{X}^{\mathrm{D}}, \mathbf{x}^{\mathrm{D}}_{\mathrm{tg}}\big) = \sum_{D=1}^{n_{\mathrm{design}}} \frac{1}{2}\|\boldsymbol{d}^D\|_2^2$
Design variables:	Material positions $\boldsymbol{X}^D$ of the design nodes
State equation:	Motion $\boldsymbol{\varphi} : \mathbf{X}^{\mathrm{D}} \in \mathcal{B}^{\mathrm{h}}_0 \rightarrow \mathbf{x}^{\mathrm{D}} \in \mathcal{B}^{\mathrm{h}}_{\mathrm{t}}$

Yet, the earlier introduced discretized deformation gradient in Eq. 10 performs the mapping of the difference vectors from the spatial to the material configuration as a smoothed gradient $\tilde{\boldsymbol{F}}$. Eq. 12 introduces an element-wise deformation gradient which is evaluated on the integration points. To obtain the smoothed deformation gradient $\tilde{\boldsymbol{F}}^D$ for a certain node, all adjacent elements are evaluated and smoothing techniques are applied to map quantities from integration points to element nodes. The used recovery technique is the widespread global Least-Squares (L^2-) Smoothing proposed by Hinton and Campbell [6].

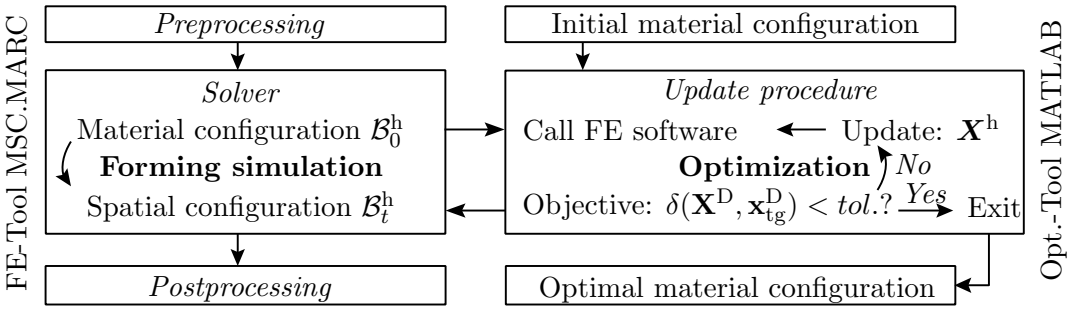

Figure 4: The iterative strategy for inverse form finding, separated into forming simulation (direct problem) and shape optimization (inverse problem) [7].

5 H-ADAPTIVE FINITE ELEMENT REFINEMENT STRATEGY

The main task of adaptive mesh refinement strategies is to control the discretization error in sense of minimization and additionally to compensate it over the area of interest. However, the quantity of the error and the area of the highest gradient is not available prior and has to be computed during the simulation [13]. Within this obstacle, particular error estimators have been established ([5], [3]).

After detecting the area of high errors or distorted elements an adaptivity strategy is applied. Typically h-, p- and r-adaption is available.

As pictured in Fig. 5(**c**) the r-refinement induces a moving of nodes by which the mesh density is concentrated to a particular place. Due to the refinement caused by a p-adaptivity Fig. 5(**b**), the polynomial degree of the element in the particular place is raised. One common used r-adaptive method is the Arbitrary-Lagrangian-Eulerian adaptivity [2].

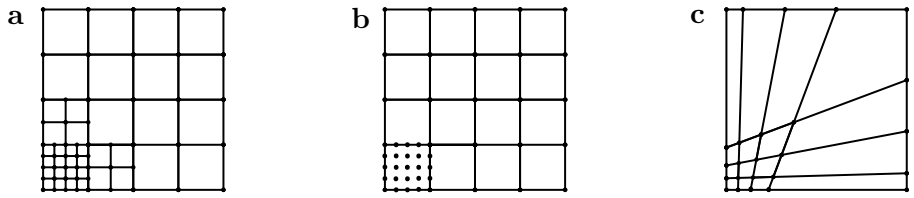

Figure 5: H-adaptivity (**a**) with a level two refinement, p-adaptivity (**b**) for one element and a global r-adapted mesh (**c**)[13]

Besides no occurrence of irregular nodes, a benefit of p- and r-adaptivity is given by no modification of connectivity during the refinement process.

H-adaption Fig. 5(**a**) means an adaption of the element size with respect to prescribed criterion, whereby the problem size rises during the implementation of new element nodes [13]. Regarding to [10], there are two different kinds of nodes within the adapted grids. The first one is the *regular* node which is standard for non adapted grids but also part of the refinement. The second is the *irregular* node generated by the refinement. The *regular* nodes are corners of the undisturbed elements. Remaining nodes are called *irregular*. By definition, all corners being part of a boundary are called *regular* nodes. As pictured in Fig. 6, the refinement of the top-right part of the structure causes some *irregular* nodes. To ensure a continuity of the solution, despite of the existence of *irregular* nodes, the solution is constrained to obtain interpolated values of surrounded *regular* nodes.

For a geometrical simple refinement depicted in Fig. 6, a mathematical description is needed, which has been introduced by [5]. Recap Eq. 16, a description between node displacement values, stiffness matrix, and node force values for one element are prescribed.

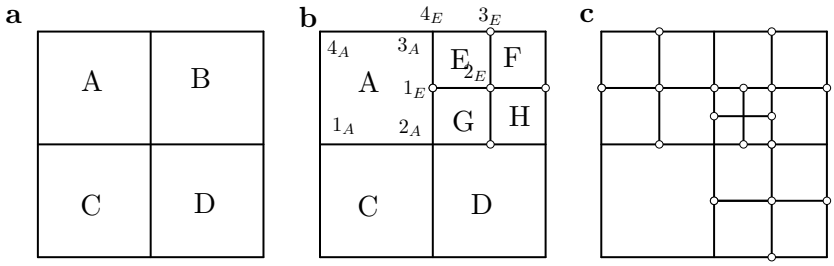

Figure 6: H-refinement of a quadrilateral element set (**a**) with level one (**b**) and level two (**c**) refinement [5].

During the refinement procedure, a 4-noded quadrilateral element is divided into four new smaller elements. Nodal values for new element nodes are required. For the newly irregular node $\mathbf{1}_E$ a relation depending on regular nodes is introduced by:

$$\mathbf{1}_E = \frac{1}{2}[\mathbf{3}_A + \mathbf{2}_A] \tag{25}$$

In conjunction with regular nodes, the transformation of nodal values is prescribed:

$$\boldsymbol{\varphi}_E = \boldsymbol{P}_E \cdot \bar{\boldsymbol{\varphi}}_E \tag{26}$$

$$\begin{bmatrix} \mathbf{1}_E \\ \mathbf{2}_E \\ \mathbf{3}_E \\ \mathbf{4}_E \end{bmatrix} = \begin{bmatrix} \frac{1}{2} & 0 & 0 & \frac{1}{2} \\ 0 & 1 & 0 & 0 \\ 0 & 0 & 1 & 0 \\ 0 & 0 & 0 & 1 \end{bmatrix} \cdot \begin{bmatrix} \mathbf{2}_A \\ \mathbf{2}_E \\ \mathbf{3}_E \\ \mathbf{4}_E \end{bmatrix} \tag{27}$$

Furthermore the variational node values $\delta\boldsymbol{\varphi}_E$ for one element are transformed with the same requirement:

$$\delta\boldsymbol{\varphi}_E = \boldsymbol{P}_E \cdot \delta\bar{\boldsymbol{\varphi}}_E \tag{28}$$

In consideration of Eq. 26 and Eq. 28, Eq. 16 is written as:

$$\delta\bar{\boldsymbol{\varphi}}_E^{\mathsf{T}} \cdot \boldsymbol{P}_E^{\mathsf{T}} \cdot \boldsymbol{K}_E \cdot \boldsymbol{P}_E \cdot \bar{\boldsymbol{\varphi}}_E = \delta\bar{\boldsymbol{\varphi}}_E^{\mathsf{T}} \cdot \boldsymbol{P}_E \cdot \boldsymbol{f}_E \tag{29}$$

Therefore, a new and again symmetric, stiffness matrix and also an updated force vector for the E-th element results in:

$$\overline{\boldsymbol{K}}_E = \boldsymbol{P}_E^{\mathsf{T}} \cdot \boldsymbol{K}_E \cdot \boldsymbol{P}_E \qquad \text{and} \qquad \overline{\boldsymbol{f}}_E = \boldsymbol{P}_E \cdot \boldsymbol{f}_E \tag{30}$$

The same procedure is applied for elements F, G and H. Subsequent, the global stiffness matrix is routinely assembled. For a second level refinement in element G in Fig. 6(**c**), element D and A has to be refined at first, otherwise two irregular nodes appear between two regular nodes, which is prohibited.

6 EXAMPLES

The iterative optimization includes a forming simulation within each step. The notch stamping process is reduced to a two dimensional and a half notch model, in order to decrease the computational costs. Symmetry conditions are applied on the right side of the model, which is depicted in Fig. 9(**a**). Beside the symmetry boundary condition, the

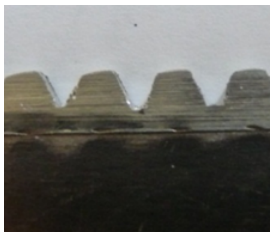

Figure 7: Workpiece of a notch stamping process as in [11]

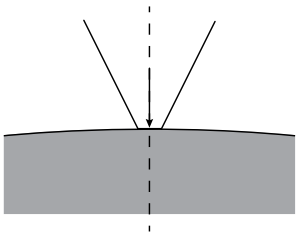

Figure 8: Sketch of the notch stamping process [11]

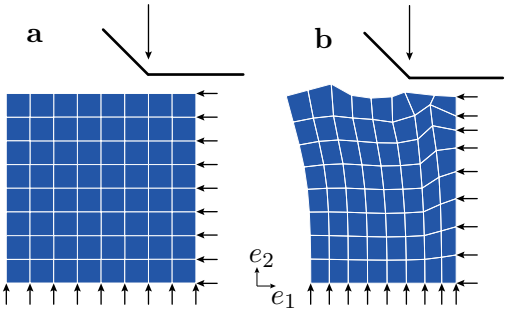

Figure 9: The original discretized material configurations (**a**) and the optimized material configuration (**b**)

bottom is fixed in e_2-direction. All four sides (width: 50 mm) of the rectangle quadratic solid body are discretized by 9 nodes, which results in 81 nodes and 64 quadrilateral elements (plane stress) for the whole model. The dual phase steel DP600 with a nonlinear

isotropic hardening and corresponding parameters, investigated by [14], is used. The notch is composed by a 12.5 mm horizontal line and a 45° line connected without a fillet radius. The resultant sharp edge is of special interest concerning the influence of the h-adaptivity to the simulation output. The initial gap between notch and solid body prevents an initial penetration during a further iteration step. A constant velocity is applied to the notch to reach a fixed solid body penetration of 25 mm. A friction factor of 0.07 is specified between the notch and the solid body. Furthermore, a contact control of the shear arctangent type is used to represent the contact behavior. This is originated by an investigation of [12] to improve the material flow during a forming process. The factor represents the application of the water based non-poisonous lubricant (Beruforge BF 150 DL) with wax particles and high viscosity. The h-adaptivity is applied with a *node in region*-option and use two regions moving along in conjunction with the notch. This constraint ensures a refinement of every element within this region and therefore includes those elements close to the notch. The configuration in Fig. 10(**a**) serves as the material start configuration of the first iteration.

The target configuration in Fig. 10(**d**) is defined by a rectangle quadratic box (width: 50 mm) that includes an exact shape of the impressed notch. A total number of 18 design nodes $\boldsymbol{X}^D$ enter the objective function $\delta(\mathbf{X}^{\mathrm{D}})$.

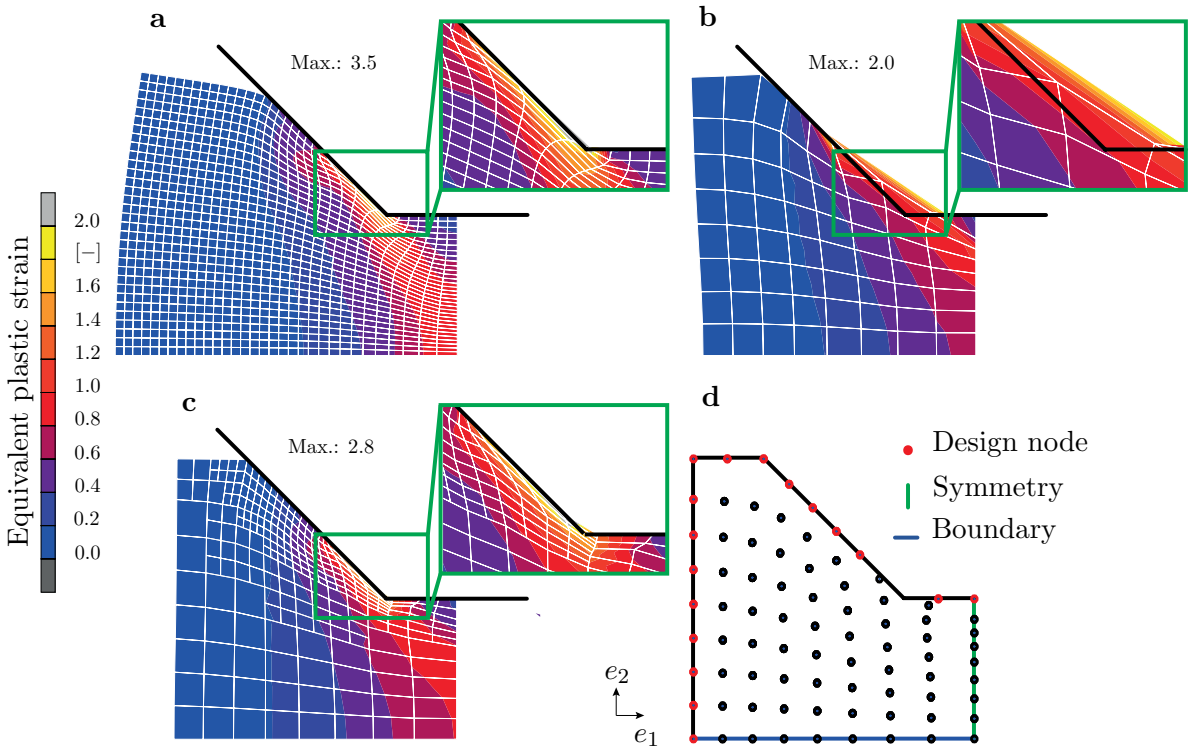

Figure 10: Deformed spatial configurations when inputting the globally refined (**a**), the optimized coarse (**b**) and the optimized h-adaptively refined (**c**) mesh, beside the prescribed target configuration (**d**)

Fig. 10 shows three examples of the deformed configuration after forming simulations. Fig. 10(**a**) is the simulation result using a refined mesh throughout the whole body without applying adaptive method. Hereby, the imprint of the notch fits proper and an h-adaptivity would not improve the result in that particular area. However, a major drawback is the excessive long computational time. The simulation takes six times longer compared to a simulation with a locally adapted coarse mesh. Consequently, adaptivity improves computational cost by factor six. Fig. 10(**b**) shows an optimized spatial configuration of a model without mesh adaptivity. The desired target configuration is not achieved. Two nodes slide along the sharp edge of the notch. As a consequence the notch penetrates the element edge. Thus, the computational results are not significant.

Finally, the spatial configuration in Fig. 10(**c**) belongs to the optimized material configuration depicted in Fig. 9(**b**). It results by applying h-adaptivity with four iteration steps. In comparison to the global mesh refinement Fig. 10(**a**) the adverse time effect is improved. In addition, compared to the coarse meshed model Fig. 10(**b**), the mesh is more accurate. The objective function, including the mean squared error of nodal differences between computed spatial and the target configuration, is thereby reduced from 5.45 (first iteration) to 0.3 (fourth iteration). This is an improvement by factor 4.6, compared to the final optimized coarse meshed model Fig. 10(**b**) with a mean squared error of 1.39.

7 CONCLUSION

An inverse form finding algorithm with material nodal positions acting as design variables is prescribed. The iterative procedure determines an optimized deformed (spatial) configuration. The commonly used h-adaptivity is applied to ensure satisfying numerical result despite of a sharp edge at the geometry of the contact body. For demonstration purposes, the shape of a semi-finished workpiece geometry, belonging to a notch stamping process, is optimized. The minimization criterion, an objective function representing the differences between the spatial computed and the target configuration, is significantly reduced. Further research will be pursued regarding mesh adaptivity in conjunction with the inverse form finding algorithm.

Acknowledgement: This work is part of the collaborative research project *Manufacturing of complex functional components with variants by using a new metal forming process - Sheet-Bulk Metal Forming* (SFB/TR73: www.tr-73.de).

REFERENCES

[1] Altenbach, H.: *Kontinuumsmechanik: Einführung in die materialunabhängigen und materialabhängigen Gleichungen.* Springer Vieweg (2015)

[2] Aymone, F., Lufs, J.: Mesh motion techniques for the ALE formulation in 3D large deformation problems. *Int. J. Numer. Methods Eng.*, **59**(14), 1879-1908 (2004)

[3] Babuvska, I., Rheinboldt, W.C.: Error estimates for adaptive finite element computations. *SIAM J. Numer. Anal.*, **15**(4), 736-754 (1978)

[4] Chenot, J.L., Massoni, E., Fourment, J.: Inverse problems in finite element simulation of metal forming processes. *Eng. Comput.*, **13**(2/3/4), 190-225 (1996)

[5] Demkowicz, L., Devloo, P., Oden, J.: On an h-type mesh-refinement strategy based on minimization of interpolation errors. *Comput. Methods Appl. Mech. Eng.*, **53**(1), 67-89 (1984)

[6] Hinton, E., Campbell, J.: Local and global smoothing of discontinuous finite element functions using a least squares method. *Int. J. Numer. Methods Eng.*, **8**(3), 461-480 (1974)

[7] Landkammer, P., Söhngen, B., Steinmann, P., Willner, K.: On gradient-based optimization strategies for inverse problems in metal forming. *GAMM-Mitt. - Special Issue: Comput. Manuf., (accepted)* (2017)

[8] Landkammer, P., Steinmann, P.: A non-invasive heuristic approach to shape optimization in forming. *Comput. Mech.*, **57**(2), 169-191 (2016)

[9] Merklein, M., Allwood, J., Behrens, B.A., Brosius, A., Hagenah, H., Kuzman, K., Mori, K., Tekkaya, A., Weckenmann, A.: Bulk forming of sheet metal. *CIRP Ann. - Manuf. Technol.*, **61**(2), 725-745 (2012)

[10] Rheinboldt, W.C., Mesztenyi, C.K.: On a data structure for adaptive finite element mesh refinements. *ACM Trans. Math. Softw.*, **62**, 166-187 (1980)

[11] Sieczkarek, P., Wernicke, S., Gies, S., Martins, P.A.F., Tekkaya, A.E.: Incipient and repeatable plastic flow in incremental sheet-bulk forming of gears. *Int. J. Adv. Manuf. Technol.*, **9-12** (2016)

[12] Vierzigmann, U., Koch, J., Merklein, M., Engel, U.: Material flow in Sheet-Bulk Metal Forming. *Key Eng. Mater.*, **Vols. 504-506**, 1035-1040 (2012)

[13] Wriggers, P.: *Nichtlineare Finite-Element-Methoden.* Berlin: Springer (2001)

[14] Yin, Q., Soyarslan, C., Güner, A., Brosius, A., Tekkaya A.E.: A cyclic twin bridge shear test for the identification of kinematic hardening parameters. *Int. J. Mech. Sci.*, **59**, 31-43 (2012)